Exploiting sparsity and field conditioning in subsurface microwave imaging of nonweak buried targets

Martina Bevacqua[1,2], Lorenzo Crocco[2,3], Loreto Di Donato[2,4], Tommaso Isernia[1,2,3], and Roberta Palmeri[1,2]

[1]Dipartimento di Ingegneria dell'Informazione, delle Infrastrutture e dell'Energia Sostenibile, Università "Mediterranea" di Reggio Calabria, Reggio di Calabria, Italy, [2]Consorzio Nazionale Interuniversitario per le Telecomunicazioni, Parma, Italy, [3]Consiglio Nazionale delle Ricerche - Istituto per il Rilevamento Elettromagnetico dell'Ambiente, Naples, Italy, [4]Dipartimento di Ingegneria Elettrica, Elettronica ed Informatica, Università degli Studi di Catania, Catania, Italy

Abstract An efficient inverse scattering strategy is proposed to achieve dielectric characterization of buried objects in lossy soils. The approach takes advantage of Virtual Experiments and Compressive Sensing to obtain quantitative reconstructions of nonweak targets which are nonsparse in the pixel representation basis, commonly adopted in microwave imaging. In addition, an original strategy is adopted to overcome the relevant information lack arising when data are gathered under aspect-limited configurations, such as in ground penetrating radar (GPR) surveys. The proposed strategy significantly outperforms the results achievable with the "state of the art" standard approaches since it allows to achieve nearly optimal reconstructions within a linear framework and without increasing the overall computational burden. Numerical examples with simulated data are given to show the feasibility of the proposed strategy.

1. Introduction and Motivations

Microwave imaging is one of the most promising candidates for accurate inspections and explorations of the underground [*Daniels*, 2004; *Pastorino*, 2010; *Persico*, 2014], thanks to its capability of quantitatively characterizing buried targets and scenarios that are not directly accessible with other sensing techniques.

However, some huge drawbacks are in order. First of all, the need to solve the underlying inverse scattering problem requires to deal with a nonlinear problem. As a result, the task has to be faced via global or local optimization strategies which entails huge limitations with respect to large computational demand (especially in case of large investigated areas) and possible lack of convergence, or even occurrence of "false solutions" [*Pastorino*, 2010].

A possible chance to avoid this difficulty is offered by linearization via Born (BA) or Rytov (RA) approximations. Although the inherent advantage to manage a linear problem, in these cases, one is usually unable to retrieve electromagnetic properties of the targets owing to the impossibility to fulfill the model assumptions. In particular, BA, so far exploited in GPR tomographic approaches, is valid only in the case of weak scatterers [*Pastorino*, 2010]. As a result, linearized inversion strategies can be properly exploited just to perform target localization [*Cui et al.*, 2001; *Habashy et al.*, 1993; *Persico*, 2014; *Soldovieri et al.*, 2007]. Furthermore, this limitation is more and more pronounced in the case of GPR surveys where data are collected just in reflection mode, especially in the case of single-frequency data processing [*Di Donato and Crocco*, 2015; *Leone and Soldovieri*, 2003]. Similar considerations hold true for the Rytov approximations [*Pastorino*, 2010].

The other main drawback in microwave imaging is concerned with the ill posedness of the problem. This latter prevents to recover high-resolution images to counteract instabilities of the tomographic imaging arising from the processing of noisy data [*Bertero and Boccacci*, 1998]. As a result, only an approximated version of the unknown profile, namely, a smooth low-energy version, can be safely recovered [*Bertero and Boccacci*, 1998].

The last drawback can be circumvented, in principle, by adopting imaging recovery approaches based on the emerging framework of compressive sensing (CS) [*Baraniuk*, 2007; *Donoho*, 2006]. It offers a powerful framework to obtain satisfactory reconstructions of "sparse images," with the possibility to achieve nearly optimal reconstruction as well as superresolution. However, CS theory has been completely assessed only in the case of linear recovery problems [*Baraniuk*, 2007; *Donoho*, 2006] so that in subsurface microwave imaging,
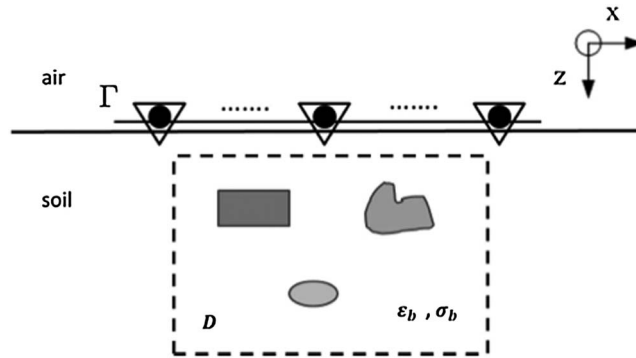
Figure 1. The geometry of the 2-D problem and the adopted measurement configuration in the paper. The black circles and white triangles represent transmitting and receiving antennas.

it has been used only in the case of weak and/or point-like scatterers [*Ambrosanio and Pascazio*, 2015]. As a matter of fact, this entails, that only few coefficients are different from zero.

In this paper we introduce, discuss, and validate a linear inversion strategy which takes advantage from the virtual experiments (VE) and a field approximation able to provide a full characterization of nonweak buried objects [*Bevacqua et al.*, 2015; *Crocco et al.*, 2012; *Di Donato et al.*, 2015] with piecewise constant electromagnetic properties. As a matter of fact, such a class of targets can be considered to be sparse when represented in terms of step functions. In a simpler fashion, one can say that their gradient is sparse in the pixel basis [*Bevacqua et al.*, 2015]. Although piecewise constant profiles do not represent the most general case, in several circumstances the targets can be assumed like stepwise homogeneous ones (for example, a mine, a stone, or a pipe). Furthermore, the proposed approach, by its very nature, allows to counteract the additional specific difficulty of working under "aspect-limited" measurements configuration, since it allows to predict the value of the field in locations other than the measurement points. As a result, it is possible to exploit a number of additional equations corresponding to specific "fictitious measurements" [*Di Donato and Crocco*, 2015].

The proposed method requires data gathered under a multiview-multistatic configuration. Although multichannel acquisitions are not the most common configuration in conventional GPR systems, it is worth noting that several emerging facilities have been developed and exploited in the last years [*Bradford*, 2008; *Francese et al.*, 2009; *Gerhards et al.*, 2008]. Moreover, in some cases, such an arrangement can be implemented also through a pair of antennas (for example, mounted on two unmanned vehicles) which gather the GPR echoes for multiple positions of the transmitter/receiver pair. On the other hand, since the method works fine with single-frequency data, the extra time paid for multichannel acquisitions is traded with the convenience of working at single frequency, avoiding the need of properly modeling the dispersivity of the soil.

The paper is structured as follows. In section 2, the scattering problem is formulated for the subsurface imaging. In section 3, an overview of the overall imaging strategy is briefly outlined with respect to the linear inversion approach based on the VE, the fictitious measurements inversion strategy, and the adopted CS recovery procedure. In section 4, a numerical analysis with simulated data for different kind of scattering systems (and soil properties) is presented to show the performance of the proposed strategy. Conclusions follow. Throughout the paper, we consider the 2-D scalar problem for nonmagnetic objects where the time harmonic factor $\exp\{j\omega t\}$ is assumed and dropped.

2. Statement of the Problem and Mathematical Formulation

As shown in Figure 1, we assume a 2-D geometry with the *y* axis as invariance direction and the electric field polarized along it. Let *D* denote the investigation domain hosting the cross section of one or more penetrable scatterers (or anomalies) with support Σ and complex permittivity $\varepsilon_s(\underline{r}, \omega) = \varepsilon'_s(\underline{r}) - j\sigma_s(\underline{r})/(\omega\varepsilon_0)$, ω being the working frequency and $\underline{r} = (x, z)$ denoting the generic point in *D*. The investigation domain is placed at a given depth (below the air-soil interface) embedded in the soil with complex permittivity $\varepsilon_b(\underline{r}, \omega) = \varepsilon'_b(\underline{r}) - j\sigma_b(\underline{r})/(\omega\varepsilon_0)$.

The region D is probed by means of antennas located on the curve Γ along the x axis, placed above the air-soil interface at given height. The antennas are modeled as filamentary currents oriented along the invariance axis. We assume that the field is gathered by all the receivers when, in turn, one antenna is transmitting and all act as receivers, that is a multiview-multistatic, i.e., multichannel, acquisition.

Under the above assumptions, the equations governing the scattering phenomenon are

$$E_s(\underline{r}_r, \underline{r}_t) = k_b^2 \int_D g_{12}(\underline{r}', \underline{r}_r) E_t(\underline{r}', \underline{r}_t) \chi(\underline{r}') \mathrm{d}\underline{r}' \quad \underline{r}_t, \ \underline{r}_r \in \Gamma, \tag{1}$$

$$E_t(\underline{r}, \underline{r}_t) - E_i(\underline{r}, \underline{r}_t) = k_b^2 \int_D g_{22}(\underline{r}', \underline{r}) E_t(\underline{r}', \underline{r}_t) \chi(\underline{r}') \mathrm{d}\underline{r}' \quad \underline{r} \in D, \ \underline{r}_t \in \Gamma, \tag{2}$$

wherein

a. $\underline{r}_r$ and $\underline{r}_t$ denote the receiver and transmitter positions, respectively;
b. E_s is the scattered field at the receiver position in the upper space;
c. E_i and E_t denote the incident and the total field in D, respectively;
d. $\chi(\underline{r}) = \varepsilon_s(\underline{r})/\varepsilon_b(\underline{r}) - 1$ is the unknown contrast function;
e. $g_{12}(\underline{r}', \underline{r}_r)$ is the external Green's function for the half-space case, i.e., the field radiated in the medium 1 (the air) by an elementary source placed in the medium 2 (the soil);
f. $g_{22}(\underline{r}', \underline{r})$ is the internal Green's function for the considered scenario, which is the field radiated in the medium 2 (the soil) by an elementary source placed in the same medium;
g. $k_b = \omega \sqrt{\mu_0 \varepsilon_0 \varepsilon_b}$ is the complex wave number of the soil, μ_0 and ε_0 being the magnetic permeability and electric permittivity in the vacuum, respectively.

Accordingly, the inverse scattering problem amounts to retrieve the unknown contrast function, which encodes the geometrical and electromagnetic properties of the targets, by solving the couple of equations (1) and (2) for given incident fields and measured scattered fields. Note that both the contrast function and the total fields of the different experiments are unknowns of the problem.

Finally, let us note that the half-space Green's functions can be easily computed solving the relevant Green-Sommerfeld integrals by means of a 1-D fast Fourier transform [*Chew*, 1995].

3. The Tomographic Imaging Problem

3.1. A Linear Approach for Nonweak Targets

In order to avoid nonlinear optimizations for quantitative imaging, we adopt the linear model proposed in *Crocco et al.* [2012]. The approach is based on a proper linear combination of the original incident (in D) and corresponding scattered fields (on Γ), in order to introduce new (virtual) experiments. Then, a novel total field approximation to effectively linearize the scattering problem, even in the case of nonweak scattering regime, is introduced.

In the following we show the basic idea of the method and extend it to the case of subsurface imaging, while addressing the reader to *Crocco et al.* [2012] for a detailed understanding of the approach.

Let us consider the scattering data equation (1). Thanks to the linearity of Maxwell equations, it can be rewritten for an arbitrary linear combination of the data problem, i.e.,

$$\Psi_s(\underline{r}_r) = k_b^2 \int_D g_{12}(r_r, \underline{r}')[\Psi_i(\underline{r}') + \Psi_s(\underline{r}')]\chi(\underline{r}') \mathrm{d}\underline{r}', \tag{3}$$

wherein the quantities denoted by Ψ are given by proper rearrangements (ruled by the same weight functions) of the corresponding fields in equation (1). Moreover, note we have explicated the total field inside the object as the sum of the incident (which is known) and the scattered (which is unknown) fields. As well known, being both χ and Ψ_s (in D) unknowns of the problem, the latter is still nonlinear.

The idea underlying the virtual experiments amounts to infer given expected properties on the internal field $\Psi_t = \Psi_i + \Psi_s$. As a result, the key question is how to find effective linear combinations of data to solve the problem more easily.

In this respect, a possible chance is to pursue a linear combination of the primary sources in such a way that the resulting scattered field resembles the field radiated by a point source located in a given position in D. Obviously, since all the information gathered in a scattering experiment lies in the measured anomalous field, such a rearrangement can be evaluated only via a smart preprocessing of this latter.

According to the above, this possibility can be actually brought by means of a "design equation" arising from looking (with a different perspective) at the far-field equation, a well-known equation for the solution of the inverse obstacle problem [*Cakoni and Colton*, 2006]. The latter reads the following:

$$\int_\Gamma E_s(\underline{r}_r, \underline{r}_t)\xi(\underline{r}_t, \underline{r}_s)\mathrm{d}\underline{r}_t = g_{12}(\underline{r}_r, \underline{r}_s),\tag{4}$$

where a different sampling point $\underline{r}_s$ (belonging to an arbitrary grid covering the investigation domain) is chosen for each different virtual experiment, so that ξ is a function of $\underline{r}_s$ as well. With such a choice, the function ξ will recombine the measured scattered field at a given receiver arising for the different transmitter's positions in such a way to match the field radiated by an elementary source located in the sampling point.

According to *Crocco et al.* [2012], when the sampling point is inside the scatterer's support, say it a "pivot point" $\underline{r}_p$, the total field can be conveniently approximated by means of the following expression:

$$\Psi_t(\underline{r}) \approx \Psi_i(\underline{r}) + LP\left[g_{22}(\underline{r}, \underline{r}_p)\right],\tag{5}$$

wherein at the right-hand side, the first addendum is the incident field arising in the virtual experiment and the second addendum is a low-pass version of the internal Green's function. Note that this operation avoids field singularity in the pivot point for the scattered field. It is worth to underline that this approximation takes implicitly into account the nature of the scatterer through the "weighting" function ξ. Since, in this kind of VE, the targets are forced trough the primary sources (Ψ_i) to behave like a point scatterer, we refer to it as the point source field (PSF) approximation.

Finally, by considering the field approximation (5) for a proper set of pivot points $\underline{r}_p$ belonging to the scatterer's support, we can turn the (original) multiview experiments in (virtual) multipivot ones without any significant information loss [*Crocco et al.*, 2012].

Obviously, the above linear framework has a limited range of validity, as it is based on an approximation of the internal field as well as on the validity range of the design equation [*Cakoni and Colton*, 2006]. This notwithstanding, exploiting the far-field equation (4) as a preprocessing step, ensures the possibility to cope with a class of dielectric profiles (in terms of dimension and contrast values) widely exceeding the BA, as shown in *Di Donato et al.* [2015]. Such a property is related to the nature of the field approximation (5), which is "scatterer aware" through the recombination of the data provided by ξ.

3.2. A Fictitious Measurements Strategy for Aspect-Limited Data

The virtual experiments' framework can be exploited not only to introduce the above linearized approach but also for the subsurface imaging problem at hand, to counteract the aspect limitation of data. Indeed, aspect-limited data are not sufficient to achieve quantitative characterization of the target even when the model assumptions are fulfilled, like the use of the BA in the case of weak scatterers or even assuming the exact knowledge of the internal field (this latter being an ideal case). This is due to the peculiar filtering spectral properties of the relevant integral operator [*Leone and Soldovieri*, 2003].

In this respect, the field conditioning enforced in each virtual experiment offers an original way to face such a drawback. In fact, the introduced approximation (5) provides an analytical expression for the fields in the whole domain D. Then, since the spatial behavior of the scattered field is known everywhere for each virtual experiment, one can introduce additional equations (corresponding to fictitious measurements) in order to get profit from the expected behavior of the scattered fields in locations other than Γ [*Di Donato and Crocco*, 2015]. In particular, one can enlarge the set of measurement data, by adding a set of fictitious measurements, say $\underline{r}_r^*$, located on a fictitious curve Γ^* (complementary to Γ) in such a way to restore the full aspect configuration. The value of the (virtually measured) scattered field at these fictitious locations would be obviously given by $g_{22}(\underline{r}_r^*, \underline{r}_p)$, as fictitious measurements are placed in the lower half-space.
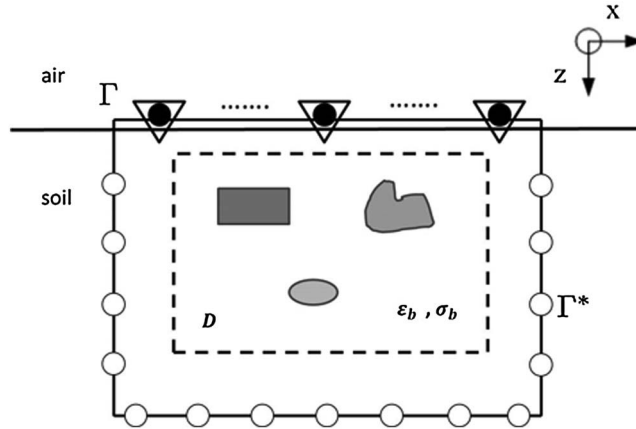
Figure 2. The virtual measurements setup. The black and white circles refer to actual and fictitious measurements, respectively, while the white triangles denote the transmitters.

According to the above, the (virtual) data equation can be suitably rewritten as follows:

$$\int_D \tilde{g}(\underline{r}', \underline{\rho}_r) \Psi_t(\underline{r}', \underline{r}_p) \chi(\underline{r}') \mathrm{d}\underline{r}' = \begin{cases} \Psi_s(\underline{\rho}_r, \underline{r}_p) & \text{if } \underline{\rho}_r = \underline{r}_r \in \Gamma \\ g_{22}(\underline{\rho}_r, \underline{r}_p) & \text{if } \underline{\rho}_r = \underline{r}_r^* \in \Gamma^*, \end{cases} \tag{6}$$

where $\underline{r}_r$ and $\underline{r}_r^*$ denote the actual and the fictitious measurement points, respectively.

To take into account the dependence of the kernel of (6) from the different kind of measurement (the actual ones on surface and the fictitious one in the underground), the Green's function is defined as

$$\tilde{g}(\underline{r}, \underline{\rho}_r) = \begin{cases} g_{12}(\underline{r}, \underline{\rho}_r) & \text{if } \underline{\rho}_r = \underline{r}_r \in \Gamma \\ g_{22}(\underline{r}, \underline{\rho}_r) & \text{if } \underline{\rho}_r = \underline{r}_r^* \in \Gamma^* \end{cases}$$

that stands for the external or the internal Green's function depending on the measurement at hand. In Figure 2, a sketch of this circumstance is depicted with measurements placed over two vertical and one horizontal fictitious arrays, denoted with Γ^*.

Exploiting the achieved field conditioning, it could seem that one can place fictitious measurements as close as possible to the targets, i.e., inside D or even inside the scatterers. However, analytical prolongation (which allows for fictitious measurements) works fine outside the scatterers, while it becomes more critical when going inside the scatterers, wherein it may more easily fail. Hence, a convenient and more reliable choice amounts to place the fictitious probes approximately at the same distance of that between the investigated domain and the actual probes.

3.3. A Compressive Sensing-Based Approach

Compressive sensing [*Baraniuk*, 2007; *Donoho*, 2006] theory provides several tools for reconstructing sparse signals from highly incomplete sets of measurements by means of constrained l_1 minimizations. In addition, it is, in principle, capable to provide nearly optimal reconstruction of the unknown provided that the latter can be represented through a sparse basis [*Baraniuk*, 2007; *Donoho*, 2006]. As a matter of fact, in many cases dealing with real life application, the unknown contrast profile can be assumed to be piecewise constant, which entails a sparse representation in terms of step functions, or, which is the same, that it has a sparse gradient in the usual pixel representation. Under the above, it makes sense to pursue the reconstruction by means of CS tools [*Bevacqua et al.*, 2015; *Candes et al.*, 2008]. Accordingly, the inverse scattering problem can be solved by means of the following minimization scheme:

$$\min_{\chi} \{ \|\nabla_{\boldsymbol{x}} \chi\|_{l_1} + \|\nabla_{\boldsymbol{z}} \chi\|_{l_1} \} \quad \text{subject} \quad \text{to} \quad \|\boldsymbol{A}\chi - \boldsymbol{b}\|_{l_2} < \delta \tag{7}$$

where

a. χ is the N-dimensional unknown function of the problem;
b. N is the number of the pixels discretizing the region of interest;

c. $\boldsymbol{b}$ is the $K \times 1$ data vector, with $K = (M + F) \times P$, which contains the M measured scattered fields and the F fictitious ones arising in the P virtual scattering experiments;

d. $\boldsymbol{A}$ is the $K \times N$ matrix which relates the unknown to data vector, obtained by considering the PSF approximation (5) and the fictitious measurements (6);

e. $\nabla_{\boldsymbol{x}}$ and $\nabla_{\boldsymbol{z}}$ are the discretized version of the gradient along the two coordinate directions x and z. In other words, $\nabla_{\boldsymbol{x}}\chi$ and $\nabla_{\boldsymbol{z}}\chi$ are the $N \times 1$ vectors containing the forward finite differences [*Bevacqua et al.*, 2015; *Candes et al.*, 2008] of the unknown function χ.

Note that in (7), the minimization of the sum of the two norms promotes the search of solutions with sparse gradient, while the constraint enforces the data consistency below a given threshold value. Finally, let us note that the parameter δ depends on the level of required accuracy as well as on the modeling and measurements errors.

4. Numerical Analysis

To give a proof of the performances achievable by means of the proposed method, we present three numerical examples concerned with GPR surveys. In particular, our goal is to show how field conditioning achieved by properly designed virtual experiments (including fictitious measurements) and CS regularized inversion (exploiting sparseness of the gradient of the unknown) allow to achieve quantitative imaging results.

The first example consists of a wet soil whose e.m. properties exhibit a 5% random variation around the average values $\epsilon'_b = 9$ and $\sigma_b = 50\,mS/m$. It embeds two targets, the first one, having circular cross section, is a stone ($\epsilon'_s = 6$) while the second one is a plank ($\epsilon'_s = 3$) with a square cross section. The rectangular imaging domain is 0.9×0.3 m^2 wide (which corresponds to $3.6\lambda_b \times 1.2\lambda_b$) and has been discretized into 78×26 cells. The antennas ($N = M = 12$), located at the air-soil interface, are evenly spaced of about $\lambda_b/2$, and the working frequency is 400 MHz.

In the second example, two rectangular lossy targets with permittivity values representative of glass ($\epsilon'_s = 8$, $\sigma_s = 0$) and porcelain ($\epsilon'_s = 6.5$, $\sigma_s = 0$, respectively) are considered. The two objects are embedded in a dry soil whose e.m. properties exhibit a 5% random variation around the average values $\epsilon'_s = 3$ and $\sigma_b = 20$ mS/m. Even in this case, the working frequency is 400 MHz. The rectangular imaging domain is 0.9×0.3 m^2 wide (which corresponds to $2.1\lambda_b \times 0.7\lambda_b$), and it has been discretized into 44×22 cells. The probing array is made of $N = M = 8$ evenly spaced antennas.

The third example consists of three rectangular targets having the same size and different e.m. characteristics, buried in a dry soil with relative permittivity $\epsilon'_s = 4$ and conductivity $\sigma_b = 1$ mS/m. The first target is a void ($\epsilon'_s = 1$), the second target is representative of a plastic mine ($\epsilon'_s = 2.5$, $\sigma_s = 0$), and the third target has the dielectric properties of a stone ($\epsilon'_s = 6$, $\sigma_s = 1$ mS/m). The working frequency is 400 MHz. The imaging domain is a square region of side 1 m (about 2.7λ), discretized into 64×64 cells. The probing array is made of $N = M = 8$ evenly spaced antennas.

The scattered field data have been simulated with a full-wave forward solver based on the method of moments and then corrupted with white Gaussian noise. Two signal-to-noise ratio (SNR) levels have been considered, SNR = 30 dB and SNR = 10 dB.

To appraise the accuracy of the results, we use two error reconstruction metrics. The first one is the usual mean square error:

$$\text{MSE} = \frac{\|\chi - \tilde{\chi}\|^2}{\|\chi\|^2}, \tag{8}$$

where χ is the actual contrast profile and $\tilde{\chi}$ the estimated one. As this metrics is a global and synthetic parameter, it is not always suitable to evaluate the fidelity of the reconstruction of the electromagnetic properties of a single object. Such an aspect can be evaluated using the following error, i.e.,

$$\text{Err}_{max} = \frac{\|\chi\|_\infty - \|\tilde{\chi}\|_\infty}{\|\chi\|_\infty}, \tag{9}$$

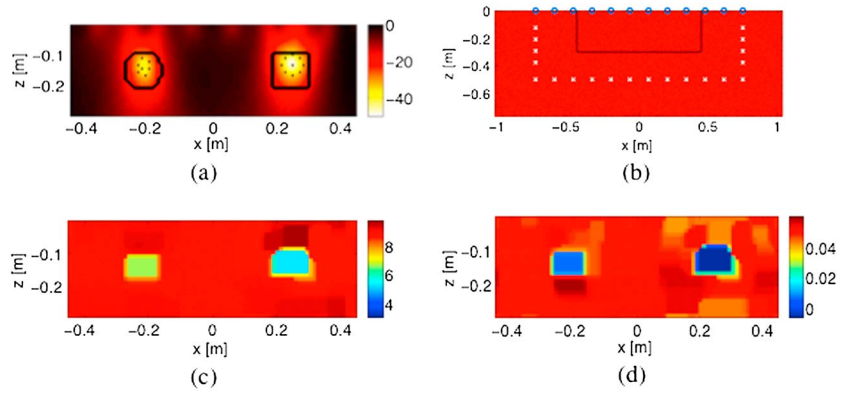where the $\|\cdot\|_\infty$ is the uniform norm.

Figure 3. Example 1. (a) Logarithmic map of the LSM indicator with superimposed the pivot points and the contour of the reference profile, (b) virtual measurements setup. (c) Permittivity and (d) conductivity of the retrieved profile by means of VE-CS ($\hat{\delta} = 0.18$) for SNR = 30 dB (MSE = 0.45, Err$_{max}$ = 0.29).

The inversion procedure consists of three steps.

The first step's goal is to reach the linearization of the scattering equation (5). In particular, we first exploit the linear sampling method (LSM) solution in order to image the support indicator and choose P evenly spaced pivot points with respect to build the multipivot experiments. The LSM indicator is given by [*Cakoni and Colton*, 2006]:

$$\Upsilon = \log_{10}\|\xi\| - \log_{10}\|\xi\|_{max}, \tag{10}$$

where $\|\xi\|_{max}$ represents the maximum value of the norm of ξ. Note that the indicator (10) assumes lower values in points belonging to the scatterers and higher values elsewhere (with respect to the overall dynamic of the energy indicator). In the case of SNR = 30 dB, the LSM indicator is shown in Figures 3a, 4a, and 5a for the three scenarios, respectively. Then, for each virtual experiment, the data equation is recast and the approximated total field is computed according to equation (5). Note that this step is computationally very efficient, as it requires only the singular value decomposition of the data matrix (whose dimensions are related to the number of transmitters and receivers).

The second step takes advantage of the achieved field conditioning by means of fictitious measurements. In practice, we add three dummy arrays with F receivers on the curve Γ^*. For the first one, both its length L_x and number of antennas are set equal to the actual array and it is placed at depth z_d from the interface.
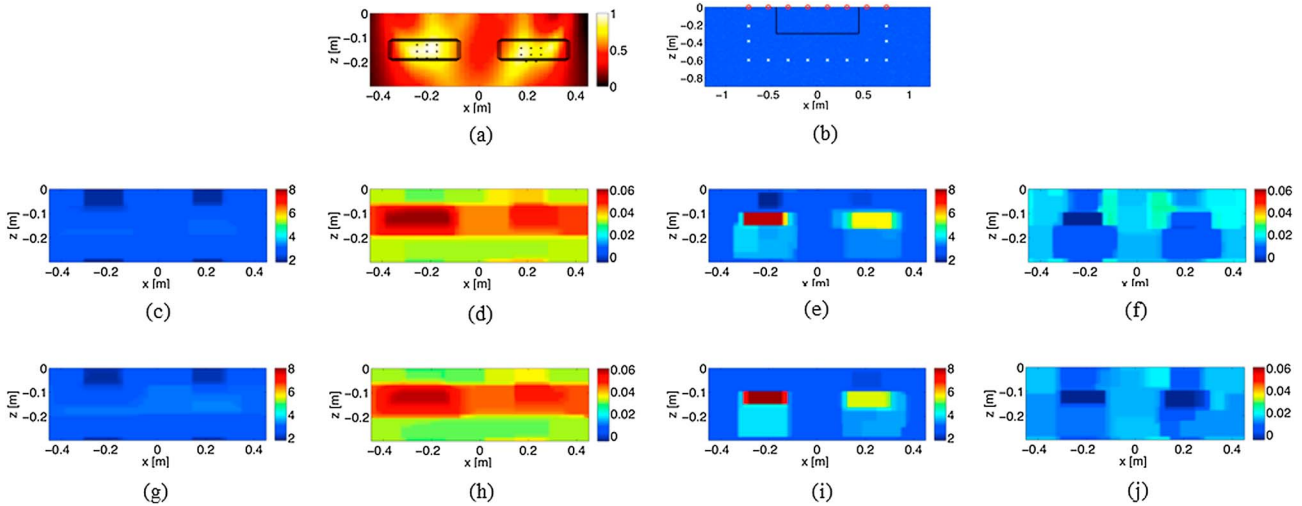

Figure 4. Example 2. (a) Logarithmic map of the LSM indicator with superimposed the pivot points and the contour of the actual profile, (b) virtual measurements setup. Permittivity and conductivity of the retrieved profile for SNR = 30 dB by means of (c and d) BA-CS ($\hat{\delta} = 0.3$) and (e and f) VE-CS ($\hat{\delta} = 0.15$). (g–j) The same as Figures 4c–4f for SNR = 10 dB with $\hat{\delta} = 0.4$ (BA-CS) and $\hat{\delta} = 0.17$ (VE-CS).
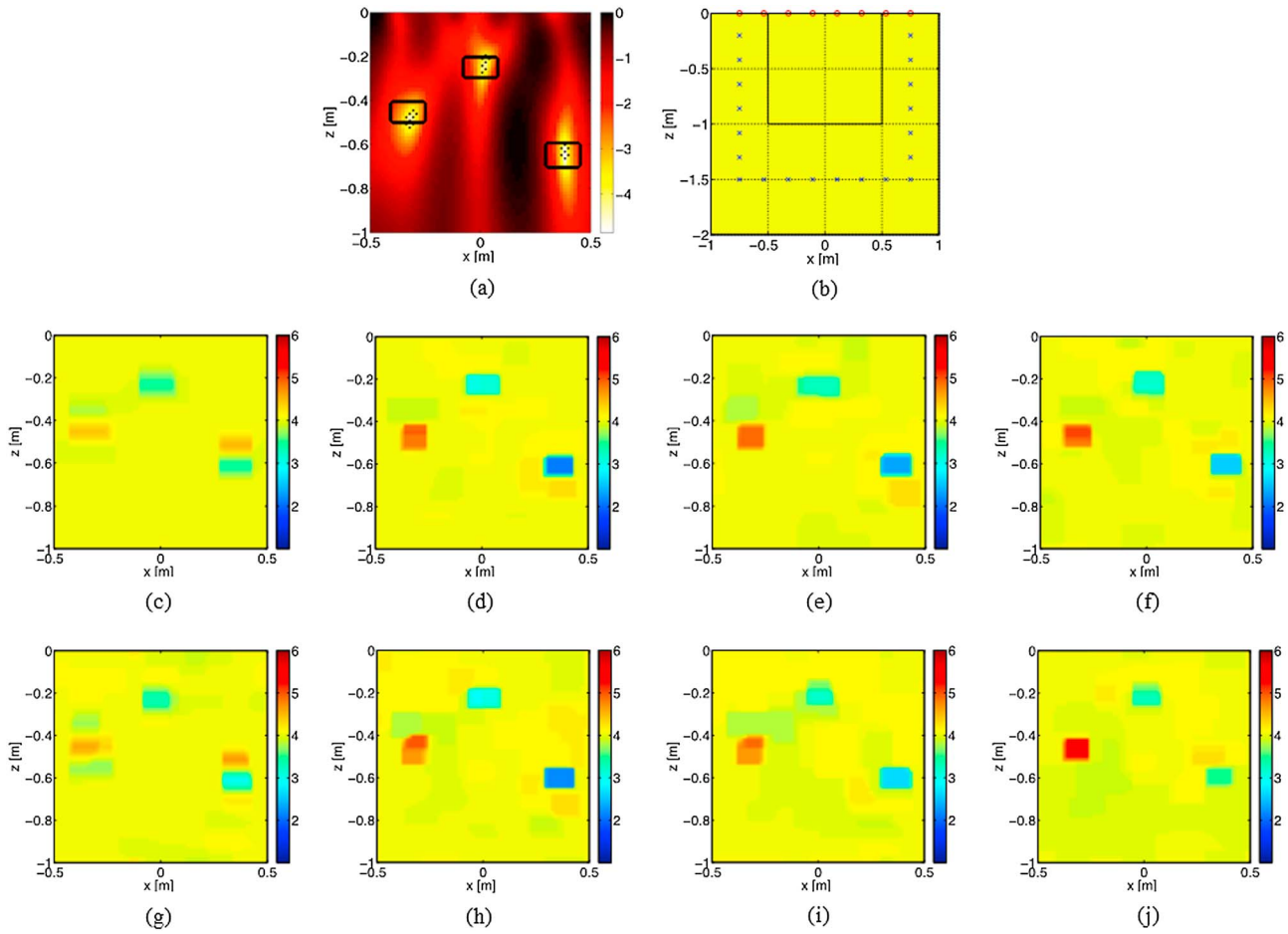
Figure 5. Example 3. (a) Logarithmic map of the LSM indicator with superimposed the pivot points and the contour of the reference profile, (b) virtual measurements setup. Permittivity of the retrieved profile by means of the CS with (c) BA ($\hat{\delta} = 0.04$), (d) VE ($\hat{\delta} = 0.32$), (e and f) VE with RF = 4 ($\hat{\delta} = 0.28$) and RF = 10 ($\hat{\delta} = 0.15$), respectively, for SNR = 30 dB. (g–j) The same as Figures 5c–5f for SNR = 10 dB with $\hat{\delta} = 0.26$ (BA-CS), $\hat{\delta} = 0.33$ (VE-CS), $\hat{\delta} = 0.28$ (RF = 4), and $\hat{\delta} = 0.24$ (RF = 10).

The second and the third virtual arrays with length z_d are placed perpendicular to the actual array. For the three scenarios at hand, the resulting configurations are shown in Figures 3b, 4b, and 5b, respectively. In particular, for the first scenario $z_d = -0.5$ m, $L_x = 1.5$ m, and $F = 20$, for the second scenario $z_d = -0.6$ m, $L_x = 1.5$ m, and $F = 12$, while for the third one $z_d = -1.5$ m, $L_x = 1.5$ m, and $F = 20$.

The last step is the optimization task via CS by means of equation (7), in which, as discussed in *Bevacqua et al.* [2015]; the tolerance parameter is set as a tradeoff between the reconstruction accuracy and the feasibility of the optimization task. To avoid the trivial solution, that is the null vector, the parameter is selected lower than $\|\mathbf{b}\|_{l_2}$, i.e., $\delta = \hat{\delta}\|\mathbf{b}\|_{l_2}$, with $\hat{\delta} << 1$.

To analyze the achievable performances of the method, we have compared the obtained results with the standard BA (Born approximation), usually adopted in tomographic GPR imaging. In particular, to carry out this comparison, possibly in conjunction with sparsity promotion tools, we have processed the simulated data also using a BA-CS approach. It is implemented using equation (7), but building the matrix **A** using the original

Table 1. Error Metrics for the Second Scenario

	SNR = 30 dB		SNR = 10 dB	
	MSE	Err$_{max}$	MSE	Err$_{max}$
BA-CS	1.42	0.62	1.39	0.65
VE-CS	0.64	0.02	0.65	0.04

Table 2. Error Metrics for the Third Scenario

	SNR = 30 dB		SNR = 10 dB	
	MSE	Err$_{max}$	MSE	Err$_{max}$
BA-CS	0.82	0.7	0.83	0.55
VE-CS	0.70	0.24	0.82	0.25
VE-CS (RF = 4)	0.69	0.35	0.84	0.38
VE-CS (RF = 10)	0.71	0.40	0.85	0.48

incident fields and noisy scattered ones instead of the proposed approach based on virtual experiments. Finally, a performance analysis lowering the numbers of processed data has been also carried out in the case of VE-CS.

Such an analysis has been carried out only for the second and the third scenarios, as the first example is reported to assess the proposed method. Results have confirmed the extended validity range of the proposed linearization based on field conditioning, as well as the remarkable advantage of using this latter in conjunction with CS, especially in the presence of a large amount of noise in the processed data, see Figures 4, 5c, 5d, 5g, and 5h. As a matter of fact, this allows obtaining reliable quantitative results both for permittivity and conductivity values (see Tables 1 and 2), outperforming the BA not only in terms of quantitative reconstruction (which is not possible at all with BA-CS) but also qualitatively.

In the third example, we have also focused our analysis on the robustness of the method against reduction of the overall number $K = 644$ of data processed. In particular, the data reduction is achieved with a routine that extract uniformly random a given number of measurements from the initial data set. Figure 5 summarizes the results obtained in this case, confirming the robustness of the CS-based procedures. Of course, for the larger noise level (SNR = 10 dB) and undersampling rate (RF = 10 and $K = 64$) the results are slightly worse as far as the estimate of the deepest target is concerned.

5. Conclusion

In this paper we have proposed a new general strategy to recover the dielectric properties of buried targets. It properly combines three different strategies, which are (i) virtual scattering experiments, which allow to introduce a field approximation which is valid for a class of scatterers wider than the weak scatterers; (ii) fictitious measurements (enabled by the enforced field conditioning), which allow to overcome information loss associated to aspect-limited data; and (iii) a recovery algorithm based on compressive sensing, in order to obtain nearly optimal reconstruction of nonpoint-like and nonweak targets.

The approach is based on a cascade of two linear steps. The first step is concerned with the solution of the design equation, which requires a low computational burden, and the computation of the virtual experiments and fictitious measurements, which in practice do not require any significant computational burden. The second step is the solution of the linearized inverse scattering problem tackled by means of a CS-based optimization routine. As a result, the overall computational burden keeps very low and is fully comparable with the commonly adopted linearized BA.

The numerical analysis has shown that the method is able to perform satisfactory characterization of buried targets having different dielectric properties in lossy soils. These preliminary results, meant to address the feasibility of the overall strategy in the subsurface imaging, encourage future work toward 3-D tomographic imaging and for testing the reconstruction capability against experimental data set.

References

Ambrosanio, M., and V. Pascazio (2015), A compressive-sensing-based approach for the detection and characterization of buried objects, *IEEE J. Sel. Top. Appl. Earth Obs. Remote Sens.*, 8(7), 3386–3395.
Baraniuk, R. G. (2007), Compressive sampling, *IEEE Signal Process Mag.*, 24(4), 118–124.
Bertero, M., and P. Boccacci (1998), *Introduction to Inverse Problems in Imaging*, Inst. of Phys., Bristol, U. K.
Bevacqua, M., L. Crocco, L. Di Donato, and T. Isernia (2015), Microwave imaging of non-weak targets via compressive sensing and virtual experiments, *IEEE Antennas Wirel. Propag. Lett.*, 14, 1035–1038.
Bradford, J. H. (2008), Measuring water content heterogeneity using multifold GPR with reflection tomography, *Vadose Zone J.*, 7, 184–193.
Cakoni, F., and D. Colton (2006), *Qualitative Methods in Inverse Scattering Theory*, Springer, Berlin.
Candes, E. J., M. Wakin, and S. Boyd (2008), Enhancing sparsity by reweighted L1 minimization, *J. Fourier Anal. Appl.*, 14(5), 877–905.

Chew, W. C. (1995), *Waves and Fields in Inhomogeneous Media*, Inst. of Electr. Electron. Eng., Inc., New York.

Crocco, L., I. Catapano, L. Di Donato, and T. Isernia (2012), The linear sampling method as a way for quantitative inverse scattering, *IEEE Trans. Antennas Propag.*, *4*(60), 1844–1853.

Cui, T. J., W. C. Chew, A. A. Aydiner, and S. Chen (2001), Inverse scattering of two-dimensional dielectric objects buried in a lossy earth using the distorted Born iterative method, *IEEE Trans. Geosci. Remote Sens.*, *39*(2), 339–346.

Daniels, D. J. (2004), *Ground Penetrating Radar*, 2nd ed., Inst. of Electr. Eng., London, U. K.

Di Donato, L., and L. Crocco (2015), Model based quantitative cross-borehole GPR imaging via virtual experiments, *IEEE Trans. Geosci. Remote Sens.*, *53*(8), 4178–4185.

Di Donato, L., R. Palmeri, G. Sorbello, T. Isernia, and L. Crocco (2015), Assessing the capabilities of a new linear inversion method for quantitative microwave imaging, *Int. J. Antennas Propag.*, *2015*, 403760.

Donoho, D. (2006), Compressed sensing, *IEEE Trans. Inf. Theory*, *52*(4), 1289–1306.

Francese, R. G., E. Finzi, and G. Morelli (2009), 3-D high-resolution multi-channel radar investigation of a Roman Village in Northern Italy, *J. Appl. Geophys.*, *67*(1), 44–51.

Gerhards, H., U. Wollschlager, Q. Yu, P. Schiwek, X. Pan, and K. Roth (2008), Continuous and simultaneous measurement of reflector depth and average soil-water content with multichannel ground penetrating radar, *Geophysics*, *73*, J15–J23.

Habashy, T. M., R. V. Groom, and B. R. Spies (1993), Beyond the Born and Rytov approximations: A non linear approach to electromagnetic scattering, *J. Geophys. Res.*, *98*(B2), 1759–1775.

Leone, G., and F. Soldovieri (2003), Analysis of the distorted Born approximation for subsurface reconstruction: Truncation and uncertainties effects, *IEEE Trans. Geosci. Remote Sens.*, *41*(1), 66–74.

Pastorino, M. (2010), *Microwave Imaging*, Wiley, New York.

Persico, R. (2014), *Introduction to Ground Penetrating Radar: Inverse Scattering and Data Processing*, Wiley, New York.

Soldovieri, F., J. Hugenschmidt, R. Persico, and G. Leone (2007), A linear inverse scattering algorithm for realistic GPR applications, *Near Surf. Geophys.*, *5*(1), 29–41.